ACS OMEGA

Open Access

http://pubs.acs.org/journal/acsodf

Article

Modification of Sugar Cane Bagasse with CTAB and ZnO for Methyl Orange and Methylene Blue Removal

Riki Subagyo, Achmad R. Diakana, Garcelina R. Anindika, Syafsir Akhlus, Hendro Juwono, Lei Zhang, Arramel, and Yuly Kusumawati*

Cite This: *ACS Omega* 2024, 9, 25251−25264

Read Online

ACCESS | Metrics & More | Article Recommendations

ABSTRACT: Sugar cane bagasse (SB) was modified with cetyltrimethylammonium bromide (CTAB), followed by impregnation with zinc oxide (ZnO) to create a synergistic adsorption and photocatalytic system for methyl orange (MO) and methylene blue (MB) removal. The presence of CTAB and ZnO was confirmed by X-ray diffraction, Fourier transform infrared, and energy dispersive X-ray (for Zn and O). Modification of SB with CTAB (CSB) generated more positive sites on the surface of SB, which enhanced MO removal compared with that of pristine SB. ZnO impregnation induces a decrease in MO removal due to the ZnO presence on the CSB surface, which might reduce the positive sites on the CSB. In addition, the positive sites on CSB can interact with Zn^{2+} and O^{2-} to form ZnO and lead to a decrease in MO removal. In contrast, the presence of ZnO facilitated good removal of MB compared to CSB, indicating that the photocatalytic process plays a greater role in removing MB. However, the addition of H_2O_2 can improve MO and MB removal under irradiation due to the formation of external •OH. The photocatalytic performance of MO and MB was also observed to be favored under acidic and alkaline conditions, respectively.

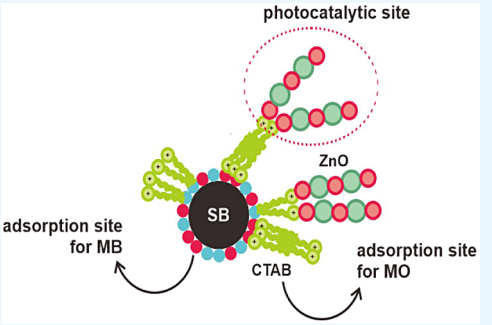

1. INTRODUCTION

Synthetic dyes are the main pollutants in wastewater discharged from textile, food, and leather industries.[1−3] The presence of colored organic compounds, such as dyes, in wastewater generally reduces the transmission of sunlight, thus impending photosynthesis and damaging aquatic ecosystems.[4] In addition, the toxic and carcinogenic properties of dyes can severely harm human beings.[5,6] Various physical, chemical, and biological methods have been adopted to eliminate dyes from contaminated waters.[7−10] Recently, photocatalysis has received much attention and is considered one of the most promising strategies to solve these problems due to its affordability, feasibility, simplicity, and pollution elimination capacity, which allows it to degrade dyes from wastewater streams. Photocatalysts involve photochemical reactions on the surfaces of metal oxide semiconductors. This requires at least two reactions to occur at the same time, namely, the oxidation reaction by holes and the reduction reaction by photogenerated electrons.[11] The positive hole and negative electron will react with oxygen and water to generate hydroxyl radicals and superoxide radical anions, and both species can degrade and mineralize stable organic pollutants.[12]

Zinc oxide (ZnO) is an n-type semiconductor that has been investigated for photocatalytic processes. ZnO possesses a band gap similar to that of titanium dioxide (TiO_2), which leads to high absorption efficiency across a large fraction of the ultraviolet (UV) spectrum.[13,14] In addition, ZnO is a promising semiconductor for green environmental management systems due to its unique properties, including a wide bandgap in the near-UV spectral region, strong oxidizing capacity, excellent photocatalytic properties, and large free exciton coupling.[15−17] ZnO crystallization and growth can also be easily controlled;[18] therefore, it has emerged as a strong candidate. Moreover, the large band gap permits ZnO to absorb only UV light (∼4% of the solar spectrum) and not visible light (∼43% of the solar spectrum),[19−21] leading to a low degradation efficiency in the solar spectrum. Therefore, many studies have reported modifications to semiconductors that involve combining semiconductors and support materials to achieve synergy between adsorption and photocatalysis,[4,22,23] therby preventing semiconductor coagulation and facilitating photocatalyst separation.[24] For instance, Calzada et al. reported ZnO-supported SBA-15 preparation by an incipient wetness impregnation technique, and the photocatalysis exhibited high photocatalytic efficiency (99%) for methylene blue

Received: March 27, 2024
Revised: May 12, 2024
Accepted: May 16, 2024
Published: May 28, 2024

(MB) degradation.[25] Tehubijuluw et al. also reported the deposition of ZnO on ZSM-5 by wet impregnation methods, and these photocatalysts yielded the highest photocatalytic efficiency toward MB (99%).[26] Nasrollahzadeh et al. investigated methyl orange (MO) photodegradation by ZnO/activated carbon. Their research showed low photocatalytic efficiency (~20%) toward 25 mg L^{-1} MO solution due to the negative charges on the surface of the composite, which led to repulsion between the negatively charged surface and negatively charged MO.[27]

Biomasses based on agricultural waste have become promising materials for supporting ZnO for MO and/or anionic molecules (AMs) removal to enhance the photocatalytic ZnO/support material for MO and/or AMs. Using renewable resources and agricultural wastes as adsorbents for pollutant removal in contaminated water is a strategy that benefits water campaigns for the environment and sustainable development.[28] Sugar cane bagasse (SB) is the waste product generated after the extraction of sucrose-containing juices from sugar cane. SB is the most productive crop residue and is composed of cellulose (35−59%), hemicellulose (18−26%), and lignin (16−25%), and it has been widely utilized for the production of fuels, surfactants, activated carbon, and adsorbents.[29] SB contains hydroxyl and carboxylic acid groups; therefore, it is an efficient adsorbent for pollutant removal. For instance, Zhang et al. reported on ball mill-modified SB, which facilitated 80% Congo Red removal at a dosage of 8 g L^{-1}.[30] The adsorption efficiency of SB can be increased by modifying SB with surfactants to improve its wettability and reduce its surface tension, which allows for the adsorption of various organic pollutants, such as phenolics, oil, and anionic dye effluents.[31,32] In addition, cetyltrimethylammonium bromide (CTAB) is less toxic to the ecosystem.[33] Rovani et al. synthesized silica nanoparticles derived from SB ash and modified them with CTAB.[34] Silica/CTAB exhibited excellent adsorption efficiency and high capacity for bisphenol A (BPA) degradation due to the hydrophobic nature of the CTAB micelles, which favor the dissolution of BPA. CTAB was employed as well to modify hectorite, resulting in increased surface area and a significant number of active sites.[35] As a result, CTAB-modified hectorite outperformed pristine hectorite in terms of adsorption performance by approximately 10-fold. Recently, Asranudin et al. reported the fabrication of hectorite-CTAB-alginate composites in the form of beads.[36] These strategies improved the adsorption performance toward MO, which was approximately 10 times greater than original hectorite beads. A summary of CTAB-modified absorbents demonstrates that CTAB stimulates the improvement of the adsorption characteristics of the adsorbent, resulting in increased adsorption performance.

Based on this observation, we developed ZnO modified with SB, which was first modified with CTAB. SB was collected from a sugar cane juice seller in Keputih, Sukolilo, Surabaya. The utilization of SB enhances the value-added SB in order to reduce the number of SB wastes. CTAB modifies the surface of SB by the interlayer formation, as confirmed by X-ray diffraction (XRD) results. The impregnation of ZnO onto CTAB-modified SB (CSB) alters the surface of CSB and changes the photon absorption profile, which is active as a photocatalyst. We also provide the proposed mechanism of the formation of CSB and ZnO-modified CTAB-SB (ZCSB) to demonstrate the interaction of SB, CTAB, and ZnO in detail. The adsorption performance of CSB and ZCSB was evaluated in batch adsorption experiments. The photocatalytic activity of the composite was also investigated under UV-LED irradiation, and MO and MB were used as the model pollutants due to their anionic and cationic nature, respectively. The optimization of ZnO loading, dosage, pH and the presence of H_2O_2 were also investigated.

2. RESULTS AND DISCUSSION

2.1. Vibrational Analysis. The vibration modes of the samples were determined using Fourier transform infrared (FTIR) spectroscopy. The IR spectra of the samples are displayed in Figure 1. All samples showed the presence of the

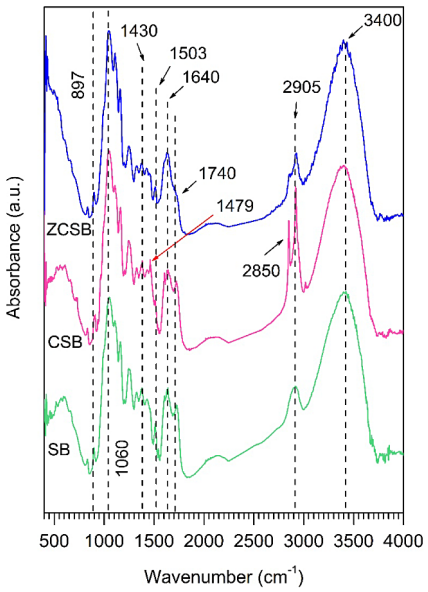

Figure 1. IR spectra of samples. SB (green), CSB (pink), and ZCSB (blue).

main cellulose absorption bands at 3400, 2905, 1740, 1640, 1503, 1430, 1060, and 897 cm^{-1}. The absorption band at 3400 cm^{-1} was attributed to the stretching vibration of the O−H, which corresponded to the strong hydrogen bonding in the sample. A stretching mode vibration for C−H was observed at 2905 cm^{-1}. The absorption band at 1740 cm^{-1} was attributed to the stretching mode vibration of C=O, corresponding to the carbonyl and carboxyl functional groups in the hemicellulose structure.[37] Skeletal aromatic ring vibration was observed at 1503 cm^{-1}.[38] The absorption band at 1430 cm^{-1} corresponded to the bending vibration of symmetric CH_2. The strong absorption band at 1060 cm^{-1} was assigned to the C−O stretching vibration, characteristic of lignocellulosic materials.[39] The sharp absorption band at 897 cm^{-1} was associated with the β-glucosidic linkage between sugars.[40] Following CTAB modification, new absorption peaks were observed at 2850 and 1479 cm^{-1}. The first absorption peak was ascribed to the C−H symmetric vibration of CTAB, and the second absorption peak was associated with the CH_3 vibration in the CTAB-modified SB, indicating the presence of ammonium salt in the samples. ZCSB also exhibited an absorption band at 2850 cm^{-1}, indicating that CTAB was retained even after impregnation with ZnO. The intensity of the absorption bands after ZnO impregnation decreased due to the reaction between CTAB, Zn^{2+}, and O^{2-}. However, the absorption band for Zn−

https://doi.org/10.1021/acsomega.4c02938
ACS Omega 2024, 9, 25251−25264

O−Zn was not clearly observed due to an overlapping band at 800−400 cm^{-1}.

2.2. XRD Analysis. As shown in Figure 2, all samples exhibited diffraction patterns for native cellulose at 2θ = 15.3°,

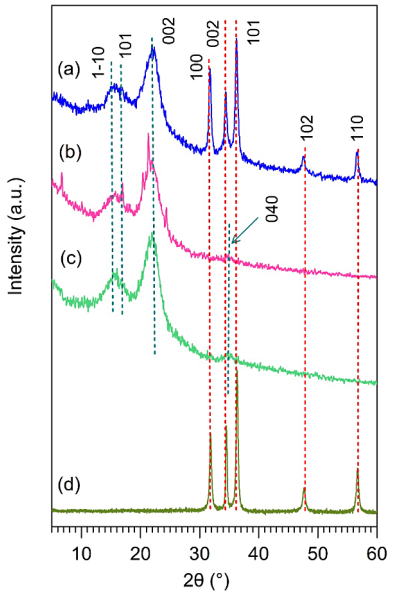

Figure 2. Diffraction patterns of (a) ZCSB, (b) CSB, (c) SB, and (d) the coprecipitation product. The vertical red and green dashed lines are the typical peaks of ZnO and cellulose with their corresponding planes.

16.2°, 21.8°, and 34.9°, which were associated with the (1−10), (101), (002), and (040) planes, respectively.[41,42] The peaks at 2θ = 15.3° and 16.2° were observed as one broad peak, similar to the previous study reported by French[43] because of the small crystallite size.[44] Compared with the tunicate standard of cellulose, the peaks about 23° shifted to 21.8°, revealing small changes in the unit cell dimensions, especially the *a*-axis that has become significantly longer.[45] Following CTAB modification, the peaks at 2θ = 15.3°, 16.2°, and 21.8° shifted to 15.9°, 17.0°, and 21.5°, respectively. The shifted peaks indicated the successful formation of interlayer spaces on the SB surface.[46] However, after CTAB modification, the peak intensity at 2θ = 34.9° decreased due to the presence of CTAB on the SB surface. ZnO impregnation on the CSB surface resulted in characteristic peaks for the wurtzite form of ZnO at 2θ = 31.785°, 34.352°, 36.297°, 47.566°, and 56.741°, which corresponded to the (100), (002), (101), (102), and (110) planes, respectively, according to JCPDS No. 36−1451. The coprecipitation product also exhibited the typical peak of wurtzite ZnO, indicating that ZnO is easily produced via coprecipitation at low temperatures. The analysis using the Debye−Scherrer equation yielded a ZnO crystallite size of 26.5−58.2 nm. The lattice parameters "a" and "c" for ZnO were estimated to be 0.3251 and 0.5221 nm, respectively. Compared with the standard data from JCPDS No. 36−1451, the lattice parameter was slightly higher, which might be due to the influence of experimental conditions on ZnO synthesis. ZnO impregnation also caused peak loss at 2θ = 34.9° because the peak overlapped with the ZnO peak. However, the other peaks that were characteristic of sugar cane bagasse were retained after ZnO impregnation.

2.3. Morphology Analysis. Figure 3 shows the morphologies of SB, CSB, and ZCSB using scanning electron

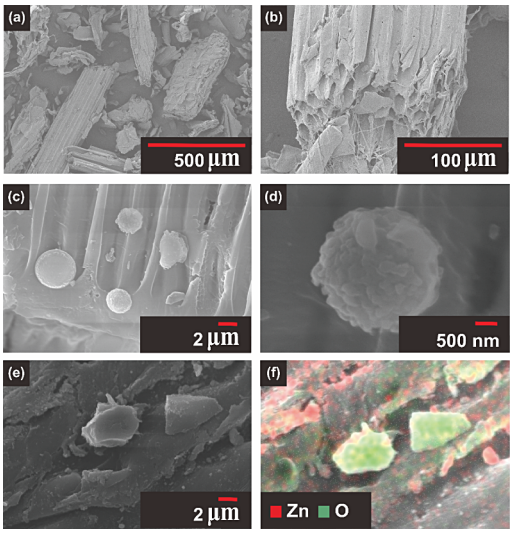

Figure 3. SEM micrographs of (a,b) SB, (c,d) CSB, (e) ZCSB, and (f) EDX of ZCSB.

microscopy (SEM). SEM analysis of SB displayed an aggregated and rough morphology, indicating the presence of lignin, hemicellulose, and other noncellulosic compounds. CSB showed the presence of CTAB molecules on the surface of SB. CTAB molecules formed chip-like structures with rough surfaces. The distribution of CTAB on the SB surface was not uniform. However, the rigid, rough, and aggregated surface of SB was retained even after CTAB modification. After ZnO was impregnated on the CSB surface, ZnO agglomerates were observed on the surface of CSB, as shown in the SEM image in Figure 3e. The clumped molecules on the CSB surface were $Zn(OH)_2$ particles. These phenomena can be described by the effect of the electrostatic forces that form ZnO and the high surface energy that is common during the synthesis process.[47] According to the energy dispersive X-ray (EDX) analysis in Figure 3f, Zn and O were clearly visible. The weight percentages of Zn and O were 8.6% and 91.4%, respectively. The high percentage of O was due to the contribution of O from compounds in the SB, such as hemicellulose, lignin, and other noncellulosic substances, as mentioned before. The presence of Zn and O in the EDX analysis also confirmed the presence of ZnO and $Zn(OH)_2$ on the CSB surface.

2.4. X-Ray Photoelectron Spectroscopy (XPS). The element compositions of SB, CSB, 10ZCSB, and ZnO were determined using XPS analysis, as depicted in Figures 4 and 5. The C 1s spectra of SB, CSB, and 10ZCSB (see Figure 4a−c) contain five deconvoluted peaks at 285.4, 286.4, 287.4, 288.6, and 290 eV, which correspond to sp^2, C−C/C−H,[48] C−O,[49,50] C=O (carbonyl),[48] and COO (carboxyl),[51] respectively. Interestingly, the peak at 287.4 in C 1s spectra of CSB is higher than that of SB due to the existence of C−N groups after the addition of CTAB. Following the impregnation of ZnO on CSB, the five deconvoluted peaks shifted toward higher binding energy, suggesting that the presence of ZnO on the CSB surface triggered electron redistribution in the composite. In the O 1s spectra, SB and CSB exhibit two peaks at 533 and 535 eV, corresponding to C−O/C=O and O−H, respectively.[52−54] The impregnation of ZnO on CSB

https://doi.org/10.1021/acsomega.4c02938
ACS Omega 2024, 9, 25251−25264

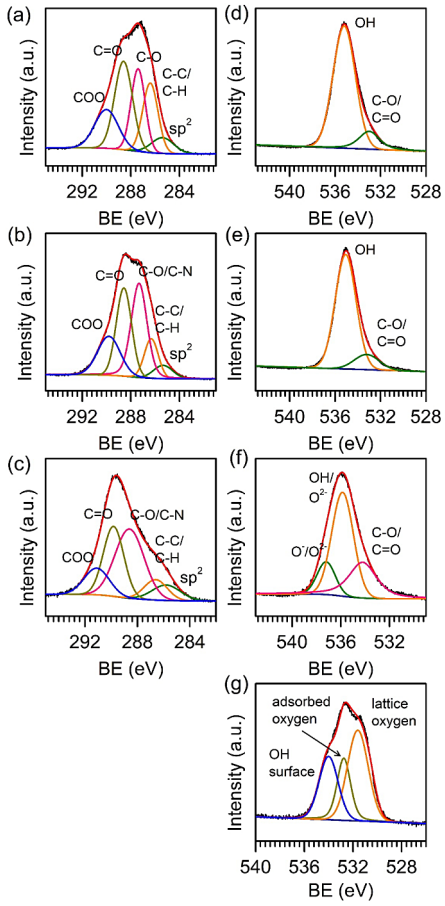

Figure 4. (a–c) C 1s and (d–g) O 1s XPS spectra of samples, including (a, d) SB, (b, e) CSB, (c, f) ZCSB, and (g) ZnO.

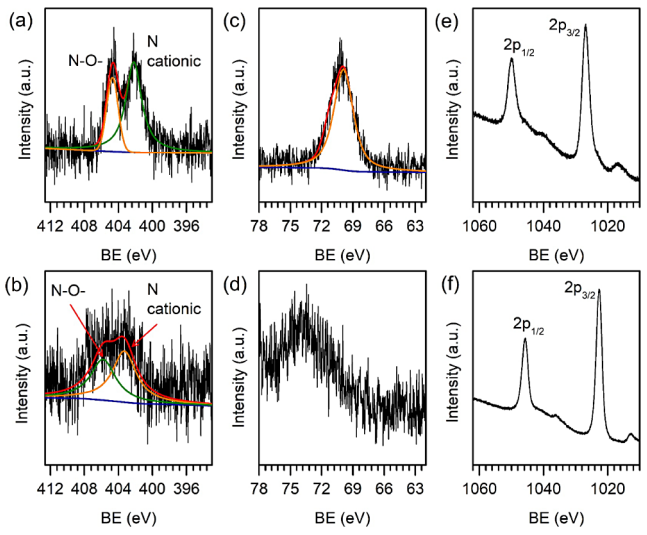

Figure 5. N 1s, Br 2p, and Zn 2p XPS spectra of the samples, including (a, c) CSB, (b, d, e) ZCSB, and (f) ZnO.

yields three peaks at 534, 535.8, and 537.2 eV. The peaks at 534 and 535.8 eV are associated with the presence of C−O/C = O and O−H, respectively. The existence of O−H might also be attributed to O−H in SB and Zn−O−H. In addition, the peak at 535.8 eV can be correlated with the O^{2-} ion in Zn−O bonding.[55] A new peak at 537.2 eV is assigned to O^{-} and O^{2-} ions in oxygen-deficient regions in the ZnO matrix.[55,56] For comparison, the O 1s spectra of ZnO show three peaks at 531.6, 532.7, and 534 eV, corresponding to lattice oxygen, adsorbed oxygen, and the OH surface.[57,58] The peak in pure ZnO appears at a lower binding energy than that in ZCSB due to the difference in electron distribution between the two. The presence of a nitrogen atom in CTAB outcomes in N 1s spectra was recorded in SCB and ZSCB as well. The peak at 402 eV corresponds to the nitrogen cation,[59] whereas the peak at 406 eV is assigned to the N−O− bond.[60] Typically, the Br 2p spectra emerge from the bromide atom in CTAB. However, the Br 2p peak in ZCSB is more challenging to deconvolute since it has a lower signal than CSB. Apart from that, the Br 2p spectra moved toward higher binding energy, which is consistent with prior findings in the C 1s and O 1s spectra. Especially for ZCSB, Zn 2p spectra arise at 1010 and 1020 eV, correlating with the Zn $2p_{3/2}$ and Zn $2p_{1/2}$ in the ZnO structure.[61] This result is in line with the Zn 2p spectra of pristine ZnO, as shown in Fi5gure 55m.

2.5. Thermal Analysis. The thermal behavior of the ZCSB was investigated using thermal gravimetry analysis (TGA), which is displayed in Figure 6. The coprecipitation product was analyzed for comparison. The coprecipitation product was synthesized by mixing zinc acetate dihydrate ($Zn(CH_3COO)_2 \cdot 2H_2O$) and sodium hydroxide (NaOH) until the pH of the solution was 11. ZCSB and the coprecipitation product were found to undergo three decomposition processes. Initially, the losses in the ZCSB and the coprecipitation product were observed to be ∼11% and ∼1.33%, respectively, from 27 to 100 °C due to the evaporation of H_2O molecules, which were physically adsorbed to the surface of the samples. ZCSB showed temperature stability in the range of 100−150 °C, revealing the maximum limit up to which SB maintained its original structure before undergoing combustion to carbon, which could be observed by the large weight loss to 77.1% from 150 to 500 °C. The coprecipitation product showed a weight loss of 5.2% in the range of 100−240 °C, indicating the decomposition of organic molecules and evaporation of chemically adsorbed H_2O in the samples.[62] We observed 1.9% weight loss in the temperature range of 240−450 °C, which was assigned to a phase transition from $Zn(OH)_2$ to ZnO. The lower amount of weight loss in the coprecipitation product indicated the higher stability of the formed ZnO and confirmed the low amount of $Zn(OH)_2$ present in the coprecipitation product.

2.6. Nitrogen (N_2) Adsorption−Desorption. To investigate the influence of CTAB modification and ZnO impregnation on the textural properties of SB, N_2 adsorption−desorption was carried out, and is shown in Figure 7. N_2 adsorption using SB was increased at the beginning stage of adsorption until the end of the adsorption process. SB exhibited a type III isotherm, implying that SB was a nonporous material. A smaller hysteresis loop was observed in SB due to the capillary condensation process. The surface area of SB was 34.517 $m^2\ g^{-1}$. Modifying SB with CTAB (CSB) resulted in decreased N_2 uptake compared to SB, which revealed that the surface of SB was covered by CTAB, and this decreased the surface area (10.556 $m^2\ g^{-1}$). Decreasing the surface area of CSB indicated that a strong interaction between SB and CTAB occurred.[63] Additionally, the hysteresis loop of CSB was wider than that of SB, which was due to the tissue percolation effect from the intercalated CTAB.[35] Following ZnO impregnation (ZCSB), ZnO was deposited on the surface of CSB, and leading to an increase in the N_2 uptake of ZCSB.

https://doi.org/10.1021/acsomega.4c02938
ACS Omega 2024, 9, 25251−25264

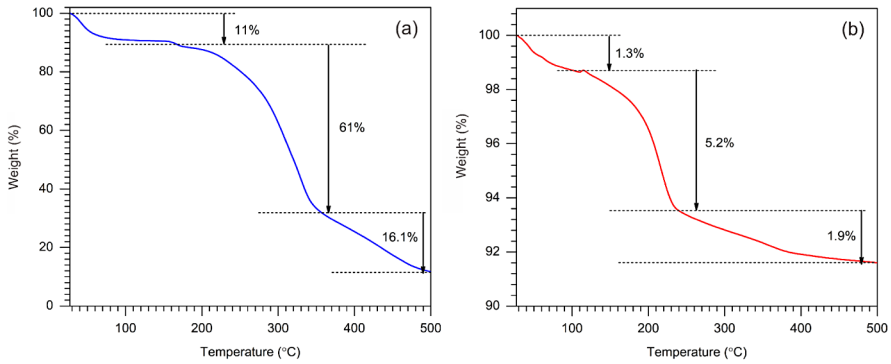

Figure 6. TGA curves of the (a) ZCSB and (b) coprecipitation product.

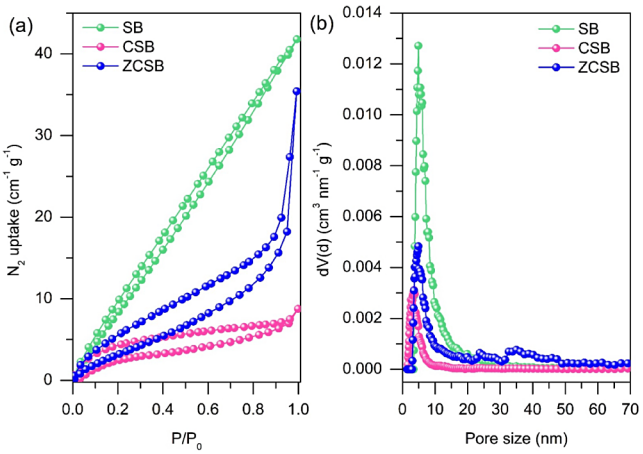

Figure 7. (a) N_2 adsorption−desorption and (b) pore distribution of the samples.

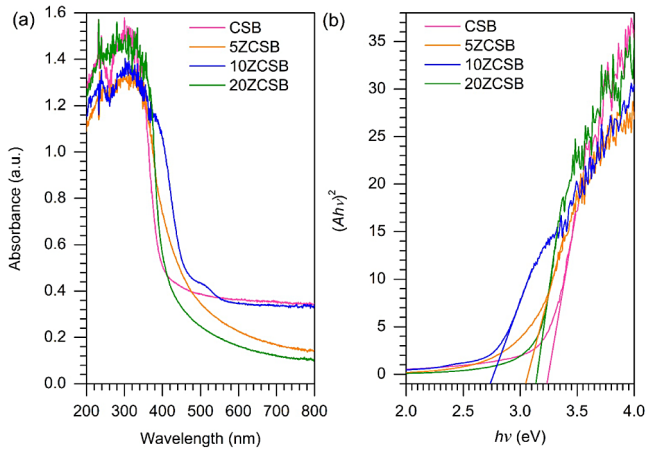

Figure 8. (a) UV−Vis spectra and (b) Tauc plots of the samples.

As a consequence, the surface area of ZCSB was improved to be 25.379 m^2 g^{-1}. Both CSB and ZCSB exhibited a type II isotherm, revealing that the samples promoted multilayer adsorption. A similar trend was also observed in the intensity of dV(d), as shown in Figure 7b. The pore diameters of SB, CSB, and ZCSB were 4.887 nm, 3.537 nm, 4.887 nm, respectively. It is important to note that the presence of pores in SB was formed due to the agglomeration of the SB particles. The addition of CTAB decreased the pore size, which was caused by the accumulation of CTAB macromolecules, reducing the formation of the pore between the SB particles. In addition, the rearrangement of particles by the formation of the interlayer also affected the pore size of CSB. Uniquely, the deposition of ZnO on CSB enhanced the pore size to be as large as that of SB, revealing that ZnO decreased the interaction between CTAB and SB and promoted the formation of the pore between particles.

2.7. Ultraviolet−visible Diffuse Reflectance (Uv−vis DR) Spectroscopy. The optical properties of the samples were investigated by UV−Vis DR spectroscopy in the wavelength range of 200−800 nm. As shown in Figure 8a, all samples absorbed wavelengths above 400 nm, which means that the samples could respond to the visible region. After ZnO impregnation of CSB, the absorption edges of the sample gradually shifted to longer wavelengths compared to CSB, changing the charge transfer pathway from CSB to ZnO, which could prevent the recombination of photoinduced electron−hole pairs.[64] The presence of ZnO on the CSB resulted in a redshift that could help adjust the bandgap and create more electron−hole pairs.[65] The Tauc plot was used to determine the band gap energy of the samples. The band gap energies of CSB, 5ZCSB, 10ZCSB, and 20ZCSB were 3.18, 3.05, 2.73, and 3.13 eV, respectively.

2.8. Proposed Mechanism of CSB and ZCSB Formation. Based on the characterization data above, the formation mechanisms of CSB and ZCSB were proposed, as shown in Figure 9. First, CSB formation potentially occurrs through the configuration of a bilayer. The monolayer could have formed through electrostatic interactions (COO^- groups in SB and protonated amine groups in CTAB) and hydrophobic interactions (aromatic rings of lignin in SB and chain tails of CTAB). The second layer may have formed due to the hydrophobic interaction between the chain tail of CTAB (tail to tail). These results indicate the presence of a large positive charge on the SB surface, thus indicating a strong ability to remove anionic contaminants (such as MO dyes) from water. The presence of Zn^{2+} cations and HO^- anions changed the bond structure between CTAB and SB in the CSB. The positive charges of CTAB on SB were bonded with the HO^- anions to form SB−CTA−OH. This chemical interaction is evidenced by the existence of N−O− bond shown in the N 1s XPS spectra depicted in Figure 5. The process continued through covalent bonding between the O and Zn atoms, followed by hydrogen capture by Br^- anions to form SB−CTA−O−Zn^+. As a result, the formation of CTA−O−Zn led to the chemical shift of the N−O−bond toward higher BE energy in the core-level N 1s spectrum of ZSCB. The positive charge on Zn^+ could further bond with HO^- anions to form SB−CTA−O− Zn−OH. This process was

https://doi.org/10.1021/acsomega.4c02938
ACS Omega 2024, 9, 25251−25264

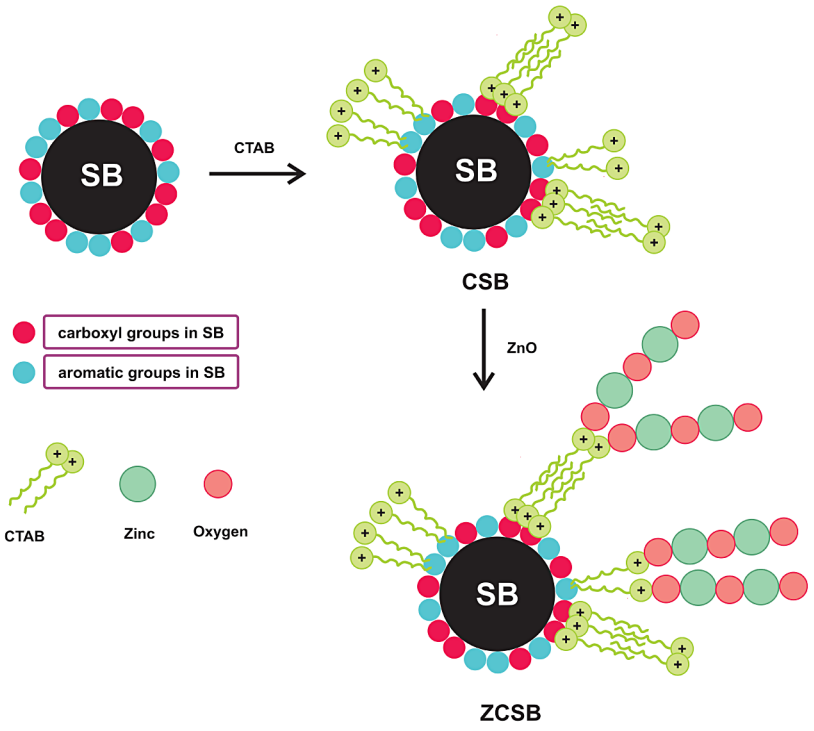

Figure 9. Proposed mechanism of CSB and ZCSB formation.

repeated to form SB−CTA−O−Zn−O−Zn−O−. However, the possibility of direct ZnO formation on the CSB surface without interactions with the positive charges of CSB via physical interactions could not be ruled out. The formation of ZnO in ZCSB is aligned with the XPS analysis that exhibits the existence of Zn 2p and O 1s spectra, revealing the presence of Zn−O−Zn and oxygen lattice that comprise ZnO. The reaction mechanism of ZCSB formation was described by the following reactions in eqs 1−3.

$$\mathrm{SB{-}CTA{-}Br + HO^{-} \rightarrow SB{-}CTA{-}OH + Br^{-}} \quad (1)$$

$$\mathrm{SB{-}CTA{-}OH + Zn^{2+} \rightarrow SB{-}CTA{-}^{2+}OZnH + Br^{-}} \rightarrow \mathrm{SB{-}CTA{-}O{-}Zn^{+} + H^{+} + Br^{-}} \quad (2)$$

$$\mathrm{SB{-}CTA{-}O{-}Zn^{+} + HO^{-} \rightarrow SB{-}CTA{-}O{-}Zn{-}OH} \rightarrow \mathrm{SB{-}CTA{-}O{-}Zn{-}O{-}Zn{-}O{-}} \quad (3)$$

2.9. Adsorption Performance of SB and CSB. Figure 10a shows the adsorption performances of SB and CSB under the same conditions. CSB showed good adsorption performance toward MO removal compared with SB at the same dosage of adsorbent. CSB exhibited an MO removal of 98.17%, while SB exhibited an MO removal of 11.38%. The presence of CTAB in SB significantly enhanced the MO adsorption performance by the formation of cationic active sites, which provided electrostatic attraction between cationic active sites and negatively charged MO. The adsorption of MO can be described by the following reaction in eq 4.

$$\mathrm{SB{-}CTA{-}Br + MO(SO_3^{-})} \rightarrow \mathrm{SB{-}CTA{-}SO_3MO + Br^{-} + Na^{+}} \quad (4)$$

The influence of CSB dosage for four amounts in the range 0.5−2 g L^{-1} was investigated at 30 min in a solution at a neutral pH (6.5). As shown in Figure 10b, the MO adsorption

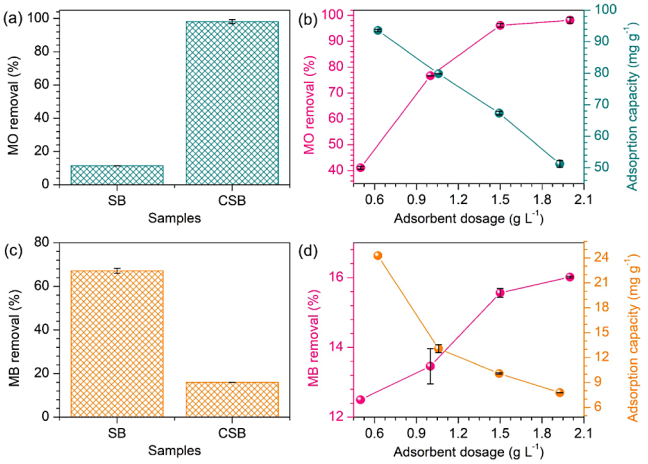

Figure 10. Adsorption performance of SB and CSB for removing MO (a) and MB (c) from the solution. (b,d) MO and MB removal due to the influence of CSB dosage.

efficiency significantly improved by increasing the adsorbent dosage from 0.5 to 1.5 g L^{-1}. MO removal via adsorption improved from 41.09 to 96.2%. Increasing the adsorbent dosage provided a high surface area and a large number of positive sites for MO adsorption. The increase in the adsorption efficiency demonstrated an increase in cationic active sites that provided more electrostatic attraction. The adsorption capacity of CSB gradually decreased with increasing CSB dosage. When adsorption reached saturation, the total amount of adsorbed MO did not change, resulting in a decline in the unit adsorption capacity. In contrast, the MO adsorption efficiency did not significantly increase at an adsorbent dosage of 2 g L^{-1}, indicating that equilibrium was attained at an adsorbent dosage of 1.5 g L^{-1}. Therefore, higher doses of adsorbent did not significantly enhance MO removal.

https://doi.org/10.1021/acsomega.4c02938
ACS Omega 2024, 9, 25251−25264

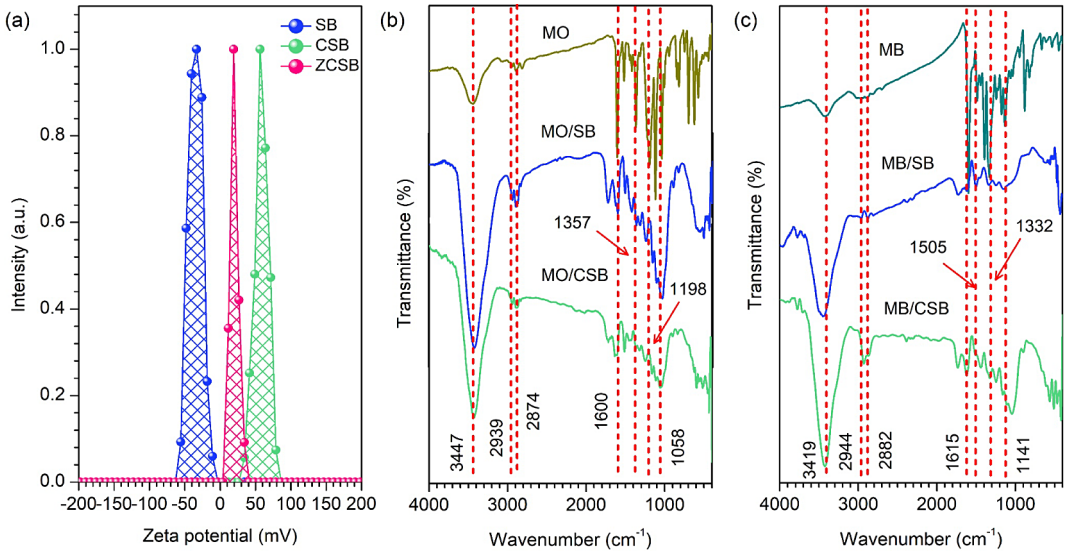

Figure 11. (a) Zeta potentials of SB, CSB, and 10ZSCB. (b, c) FTIR spectra of SB and CSB after the adsorption process with MB and MO for comparison.

In contrast, CSB has a poor adsorption performance for removing MB from the solution, but SB has a greater adsorption efficiency for removing MB. Figure 10c shows that the adsorption removal of SB and CSB in absorbing MB is 67.13% and 21.08%, respectively. Figure 10d shows that increasing the adsorbent dose improves MB adsorption removal. However, the removal percentages are still lower than those of SB. This finding suggests that the presence of CTAB on SB is detrimental to MB adsorption because the adsorption removal of CSB is lower than that of SB. Furthermore, the adsorption efficacy of SB and CSB in eliminating MO and MB yields opposite findings. We tentatively postulate that the presence of CTAB on SB resulted in a significant amount of positive surface charges. As a result, such electrostatic repulsion could facilitate tMB adsorption onto the CSB surface become unfavorable. On the contrary, the high positive surface charge promotes the MO adsorption. Based on these findings, our adsorption data unambiguously demonstrated that CTAB is a good candidate for anionic dyes like MO. The impact of the CSB dose was also investigated, as seen in Figure 10d. The changes of CSB concentration potentially enhance the MB elimination rate, facilitating a high number of active sites.

In order to strengthen the discussion, the zeta potentials of SB, CSB, and 10ZCSB are depicted in Figure 11a. SB possesses a negative surface charge, allowing MB adsorption by electrostatic attraction. Meanwhile, the negative surface charge caused repulsion with MO molecules, resulting in poor efficiency. After the addition of CTAB, the surface charge of SB became positive, promoting electrostatic interaction between MO molecules and their surface. The zeta potential results are consistent with the adsorption performance described above. In further detail, the postadsorption study of SB and CSB was performed using FTIR based on the previous reported works.[66−68] FTIR was used to investigate the interaction between SB, CSB, and dye molecules, as demonstrated in Figure 11b,c. Following MO adsorption, the primary cellulose absorption peaks in SB are more noticeable than those in CSB, indicating that MO molecules accumulated on the CSB surface. The absorption peak of C−H elongation of $-CH_2$ and $-CH_3$ at 2939 and 2874 cm^{-1} can be observed in MO/SB and MO/CSB,[69] demonstrating the accumulation of MO molecules on the SB or CSB surface. Apart from that, the existence of both C−H elongation groups in the MO/CSB also indicates that the CTAB cation was not leached during the adsorption process. The existence of an absorption peak at 1600 cm^{-1} in MO/SB and MO/CSB is due to the phenyl group vibration of the MO anion.[70] The presence of a sulfonic acid group vibration at 1058 cm^{-1} further supports the presence of MO on the SB and CSB surfaces.[70] The absorption peak at 1198 cm^{-1} is attributed to the C−N stretching vibration in MO structure.[71] On the other hand, the cellulose peak is more visible in CBS than in SB due to the smaller amount of MB molecules adsorbed on the CSB surface. Several peaks correlated to the typical MB absorption peak, including C−H elongation of $-CH_2$ and $-CH_3$, phenyl group, C−N, C=N, and C−S, are seen at 2944, 2882, 1615, 1505, 1332, and 1141 cm^{-1}, respectively.[66,69] The appearance of the typical peak of MB molecules indicates that MB has adsorbed on the surface of SB and CSB. According to IR analyses, the presence of SO_3^- in MO and $(CH_3)_3-N^+$ in MB promotes electrostatic interaction with positive and negative surface charges, respectively.[36,72] Aside from that, hydrogen bridges are generated when the hydroxyl group (OH) in SB or CSB interacts with the oxygen atom in MO's SO_3^- or the nitrogen atom in the MB.[73,74] Furthermore, the OH group facilitates n−π contact with phenyl groups in MO or MB, as evidenced by the presence of phenyl groups in the FTIR spectra following adsorption.[73]

2.10. Photocatalytic Evaluation of ZCSB. The photocatalytic evaluation of ZCSB was conducted under dark and irradiated conditions. A mixture of photocatalyst and MO was irradiated for 30 min to compare with the adsorption performance of CSB. The MO removal efficiency of 10ZCSB via the adsorption (dark) process was slightly lower compared with the adsorption efficiency of CSB under dark conditions (Figure 12a). The impregnation of ZnO on the CSB surface led to new interactions due to the presence of Zn^{2+} and HO^-, and consequently, the positive charge on the 10ZCSB decreased, which is in agreement with the zeta potential of

https://doi.org/10.1021/acsomega.4c02938
ACS Omega 2024, 9, 25251−25264

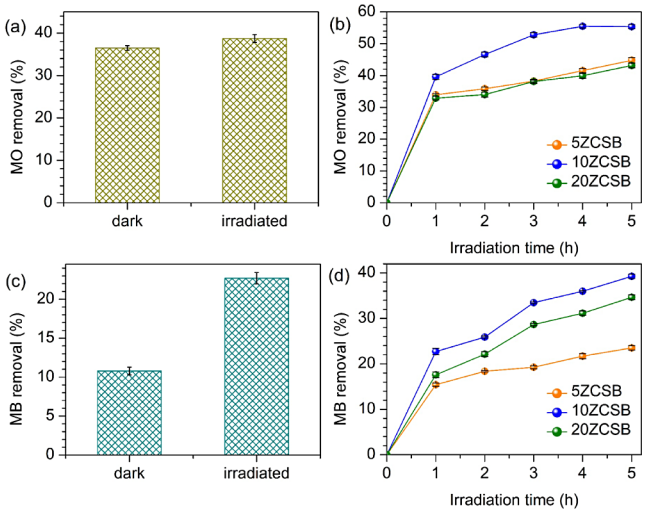

Figure 12. (a, c) he photocatalytic test of 10ZCSB in the dark and under irradiated conditions for 30 min for removing MO and MB, respectively. (b, d) The influence of the amount of ZnO on CSB for MO and MB removal, respectively.

10ZCSB in Figure 11a. The decrease in the positive sites of 10ZCSB led to a decrease in MO capture on the 10ZCSB surface and resulted in a decrease in adsorption-driven MO removal. MO removal was slightly enhanced via the photocatalytic process compared with the dark condition due to the presence of low amounts of ZnO on the surface. However, during the early stages, the adsorption process was more dominant than the photocatalytic process, which can be seen from the slight difference in efficiency. Next, we observed the photocatalytic activity of ZCSB at different irradiation times and various ZnO amounts. Similarly, the photocatalytic degradation of MB using 10ZCSB is slightly more efficient compared to the CSB. Previously, we indicated that by introducing CTAB to SB yielded a lowering its negative surface charge and thereby facilitated the adsorption performance toward MB. Following ZnO impregnation, the adsorption performance of 10ZCSB is somewhat increased by approximately 1.5% (in the same dosage) with MB removal of 17.73%. In Figure 12c, the MB removal is 11% in dark conditions, which is lower compared to CSB since only 0.02 g of adsorbent was used in this condition as a comparison to the photocatalytic results. A small number of MB interacts with radical species to destroy MB, resulting in poor photocatalytic activity of 10ZCSB. As shown in Figure 12b,d, the photocatalytic activity of ZCSB increased with increasing irradiation time. 10ZCSB exhibited the highest photocatalytic activity of 55.36%, followed by 5ZCSB (44.76%) and 20ZCSB (43.15%) for removing MO in solution. In addition, 10ZCSB showed a removal gap in photocatalytic activity from 1 to 5 h of ∼16%, which was higher than that of 5ZCSB (∼11%) and 20ZCSB (∼11%). In MB photoremoval, 10ZCSB also exhibited the highest photocatalytic performance with the efficiency of 39.27%, followed by 20ZCSB (34.64%) and 5ZCSB (23.51%). Since the adsorption performance of ZCSB is lower in removing MB, MB removal under light irradiation is more prominent due to the photocatalytic process. It can be seen that the removal gap between dark and irradiated conditions is more than 2 times. Based on the results, the synergy between adsorption and photocatalysis was important for achieving efficient dye removal. With 10% ZnO impregnation, photon absorption was enhanced, and a low band gap was observed, which was advantageous for MO and MB removal. In addition, 10% ZnO impregnation retained an optimum number of positive cations on the surface, which was crucial for MO adsorption. However, the photocatalytic activity of all ZCSB toward MO and MB dyes was low compared with that reported in previous research. This result might be due to the high concentration of MO and MB used in the experiments, which reduced light penetration to the ZCBS surface, resulting in inadequate activation of the catalyst and ultimately inadequate generation of electron−hole pairs. Consequently, the concentration of •OH decreased and was insufficient for dye removal at high MO and MB concentrations. In addition, the high concentration of the MO solution led to the accumulation of MO and MB molecules on the ZCSB surface, which blocked the active sites and ultimately reduced the production of hydroxyl radicals.

To increase the photocatalytic activity of 10ZCSB, hydrogen peroxide (H_2O_2) was introduced to the MO and MB solutions under conditions similar to those of the previous photocatalytic process. H_2O_2 is an environmentally friendly oxidizing agent and has a positive effect during most photocatalytic reactions. As shown in Figure 13a, at an irradiation time of 1 h,

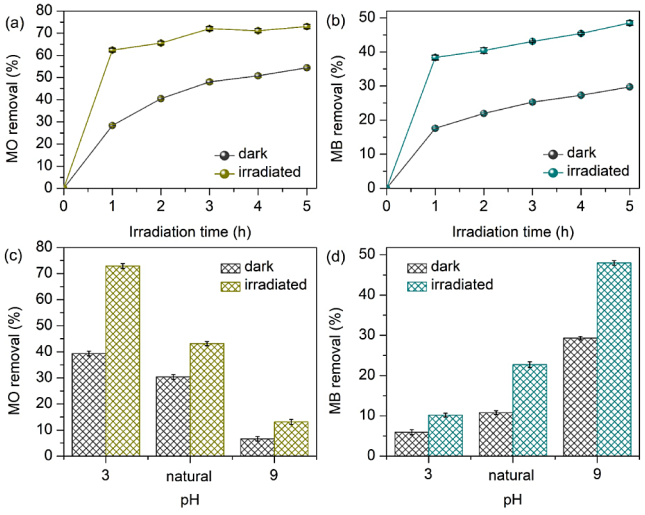

Figure 13. Influence of H_2O_2 in removing (a) MO and (b) MB. (c,d) The effects of pH solution on MO and MB removal, respectively.

the photocatalytic activity of 10ZCSB increased from 39.57% to 62.57% after the addition of H_2O_2 for MO removal, and the photocatalytic activity continued to increase until irradiation for 3 h. In MB removal (Figure 13b), MB photoremoval increased from 22.69% to 38.36% after the addition of H_2O_2 at an irradiation time of 1 h. The photocatalytic efficiency is slightly increased by increasing the irradiation time. With the addition of H_2O_2, hydroxyl radicals were formed by the following reactions in eqs 5−7:[75]

$$H_2O_2 + e^- \rightarrow {}^{\bullet}OH + OH^- \quad (5)$$

$$H_2O_2 + h\nu \rightarrow 2{}^{\bullet}OH \quad (6)$$

$$H_2O_2 + {}^{\bullet}O_2 \rightarrow {}^{\bullet}OH + OH^- + O_2 \quad (7)$$

During the photocatalytic process, the addition of H_2O_2 as an external oxidizing species can suppress the recombination of electron−hole pairs, increasing the MO and MB removal rate.

https://doi.org/10.1021/acsomega.4c02938
ACS Omega 2024, 9, 25251−25264

However, the photocatalytic activity at irradiation times of 4 and 5 h was not significantly different from the irradiation process at 3 h. The addition of excess H_2O_2 leads to a level of •OH formation that exceeds the level of hole formation, thereby reducing the photocatalytic efficiency. In addition, the excessive formation of •OH caused the formation of the less reactive radical $HO•_2$ by the following reaction in eqs and 89:[76]

$$H_2O_2 + {}^{\bullet}OH \rightarrow H_2O + HO^{\bullet}_2 \quad (8)$$

$$HO^{\bullet}_2 + {}^{\bullet}OH \rightarrow H_2O + O_2 \quad (9)$$

The photocatalytic rate was controlled by the electron−hole recombination rate. Excessive H_2O_2 addition scavenges radical species by recombining with the dissociated hydroxyl radicals and leads to a decrease in the photocatalytic rate.

The photocatalytic process can be affected by the pH of the MO solution, which influences the MO and MB molecule attachments to the ZCSB surface. As shown in Figure 13c, MO removal increased to 72.9% at an acidic pH by using 10ZCSB as a photocatalyst. Under basic conditions, the MO removal decreased to 13%. A similar result was obtained in the dark; the highest MO removal occurred at an acidic pH. MO is an anionic dye and has N−H groups. Under acidic conditions, 10ZCSB is protonated and saturated with H^+, facilitating MO adsorption via strong electrostatic attraction between the positively charged catalyst surface and negatively charged MO molecules, followed by the photocatalytic reaction of MO on the surface of 10ZCSB, which enhances MO removal. Under alkaline conditions, the poor MO removal observed was due to competition between OH^- and MO^- present in solution. In contrast, 10ZCSB has the maximum photocatalytic activity in eliminating MB under basic conditions with an efficiency of 47.98%, which decreases to 10.17% under acidic conditions (see Figure 13d). At alkaline conditions, the surface of 10ZCSB is saturated with OH^-, which induces the electrostatic attraction of MB cationic and improves MB adsorption on the 10ZCSB. Under light irradiation, the radical active species undergoes a photocatalytic process to eliminate the adsorbed MB molecule on the surface of 10ZCSB. On the contrary, the adsorption competition between H^+ and MB^+ occurs in acidic conditions. As a result, the adsorption performance of 10ZCSB is extremely poor, resulting in a low photocatalytic activity toward MB.

The influence of the ionic strength on photocatalytic activity was also investigated in order to imitate the natural wastewater matrix. Figure 14a shows that the existence of natrium chloride (NaCl) and natrium carbonate (Na_2CO_3) has no effect on 10ZCB's photocatalytic efficacy in removing MO from solution. Interestingly, the addition of natrium nitrate ($NaNO_3$) has a modest effect on the photocatalytic efficiency of 10ZCSB by reducing the level of MO elimination. The presence of NO_3^- increased the adsorption competition between NO_3^- and MO. As a result, NO_3^- consumes holes, inhibiting 10ZCSB's photocatalytic activity toward MO. In the MB system, the presence of NO_3^-, Cl^-, and CO_3^{2-} can be easily adsorbed into the surface of 10ZCSB since 10ZCSB has a positive surface charge. As a consequence, the adsorption of MB on 10ZCSB was decreased, lowering the amount of MB molecules eliminated by radical active species. Therefore, MB removal by 10ZCBS is reduced in the presence of NO_3^-, Cl^-, and CO_3^{2-}. Previously, Degrabriel et al. reported that the photocatalytic performance of TiO_2 was reduced due to the existence of Cl^-.[77] They suggested that the decreasing performance of TiO_2 was due to the direct interaction of Cl^- with the active species during the photocatalytic process. Similarly, Mul's group also reported that the presence of Cl^- and NO_3^- inhibited the photocatalytic activity of TiO_2.[78]

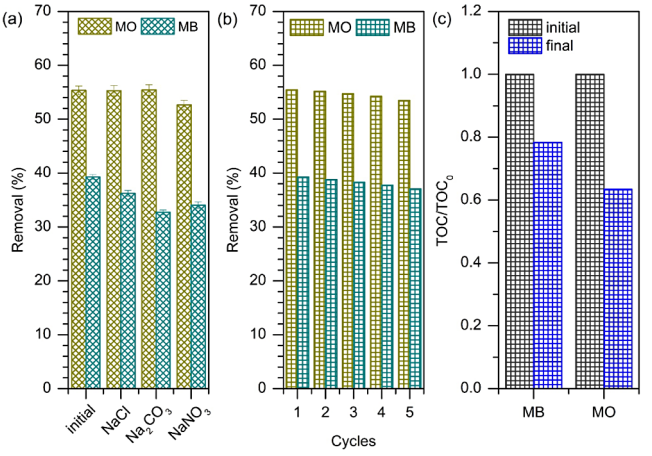

Figure 14. (a) Influence of ionic strength in removing MO and MB. (b, c) The reusability study and TOC analysis, respectively.

The reusability study of 10ZCSB to remove MO and MB in solution was also performed. As shown in Figure 14b, the photocatalytic performance of 10ZCBS is slightly decreased until the fifth cycle of the photocatalytic process. This result implies that 10ZCSB has good performance to remove MO and MB. The mineralization analysis using TOC-VCSH Shimadzu (Japan) was carried out to support the photocatalytic results (see Figure 14c) in order to calculate the degree of mineralization.[79−82] It can be seen that the total organic compound (TOC) value of the MB or MO final solution was reduced compared to the MB or MO initial solution, respectively. The decrease of the TOC value of MB is lower compared to the decrease of the TOC value of MO, which is in line with the photocatalytic results.

2.11. Economic Analysis. The economic analysis was conducted to determine the cost of producing the adsorbent photocatalyst. The economic analysis was conducted by calculating the cost of material production from SB to CSB and ZCSB. Because SB is obtained from a juice merchant, the cost is nothing. However, in large-scale production, SB may be obtained at a reasonable cost, estimated to be between 2 and 3 USD per kilogram. The conversion of SB to CSB and ZCSB requires many ingredients, which are stated at around 300 USD per kilogram of SB utilized. The overall cost of generating these materials is 303 USD/kg, which is the price for large-scale production. However, at the lab scale, material production is just 5%, resulting in a manufacturing cost of 15−16 USD. In addition, its generated features are suitable for eliminating dye wastewater, specifically anionic dyes type, including Remazol, Indigosol, and naphthol.

3. CONCLUSION

CTAB-modified SB (CSB) was successfully synthesized, followed by impregnation with ZnO (ZCSB). SB, CSB, and ZCSB were investigated for the decolorization of MO and MB dyes. The presence of CTAB on SB generated more positive sites, which was advantageous for MO removal; meanwhile, CSB exhibits low efficiency for MB removal. With ZnO impregnation, the positive site on CTAB decreased due to

https://doi.org/10.1021/acsomega.4c02938
ACS Omega 2024, 9, 25251−25264

interactions of positive sites with hydroxyl anions and zinc cations to form ZnO on the CSB surface. The decrease in the number of positive sites after ZnO impregnation decreased MO removal both in the dark and under illumination. In contrast, MB removal was improved by the formation of ZCSB, indicating that the photocatalytic process is playing a role compared to the adsorption process. To increase MO and MB removal via photocatalysis, H_2O_2 was added, and it facilitated higher MO and MB removal because of the formation of external •OH, which plays a vital role in the photocatalytic system. MO removal by ZCSB was significantly enhanced under acidic conditions, whereas the photocatalytic performance of ZCSB was increased at alkaline conditions for removing MB. 10ZCBS showed good reusability until five cycles of the photocatalytic process for removing MO and MB under UV light irradiation.

4. METHODS

4.1. Materials. $Zn(CH_3COO)_2{\cdot}2H_2O$ (Sigma-Aldrich, ≥99%, Germany), NaOH (Sigma-Aldrich, ≥99%, Germany), acetone (C_3H_6O 99%, Sigma-Aldrich, ≥99%, Germany), ethanol (C_2H_5OH 99%, full time, ≥99%, Germany), CTAB (Merck, ≥99%, Germany), MO ($C_{14}H_{14}N_3NaO_3S$, Merck, ≥90%, Germany), chloride acid (HCl, Sigma-Aldrich, 37%, Germany), H_2O_2 (Sigma-Aldrich, 30%, Germany), $NaNO_3$ (Sigma-Aldrich, Germany), NaCl (Sigma-Aldrich, Germany), and Na_2CO_3 (Sigma-Aldrich, Germany). All chemicals were used without purification.

4.2. Preparation of CSB. First, SB was washed using water and dried under solar irradiation for approximately 3 days. The dried SB was cut into small pieces and then washed with aqua demineralization (aqua DM). The small pieces of SB were left overnight for 24 h. The dried small pieces of SB were broken down using a blender, sifted into a 40-mesh size, and labeled MSB. Two grams of CTAB was dissolved with aqua DM while stirring for 30 min. Five grams of MSB was added to the CTAB solution, followed by stirring for 24 h at room temperature. The solid was separated and washed by using aqua DM. The obtained solid was dried at 80 °C for 24 h. The dried solid was mashed and sifted again to obtain a uniform sample size.

4.3. Preparation of ZCSB. The preparation of CSB was carried out by a coprecipitation method. $Zn(CH_3COO)_2{\cdot}H_2O$ was dissolved in 10 mL of aqua DM, followed by constant stirring for 30 min. One gram of CSB was added to the solution and stirred for 15 min. NaOH (0.2 M) was introduced dropwise until the pH of the solution was 11. After the pH solution of 11 was reached, the mixture was stirred for 2 h. The mixture was left for 30 min at room temperature, followed by the separation process via centrifugation to obtain the solid. The obtained solid was washed until neutral and dried at 100 °C for 24 h. The amount of ZnO was varied at 5, 10, and 20% (w/w) and labeled ZCSB5, ZCSB10, and ZCSB20, respectively.

4.4. Characterization of ZCSB. The crystallite phase and structure of SB, CSB, and ZCSB were investigated by powder XRD using an 18 kW advanced X-ray diffractometer (X'pert Pro PANalytical, Netherlands) with Cu Kα radiation (λ = 1.54056 Å). FTIR spectroscopy (Shimadzu, Japan) via a KBr method was utilized to identify the configuration of the functional groups in the samples. The morphology of the ZCSB and SB was observed by SEM (S-7400, Hitachi, Japan), and EDX spectroscopy was used to examine the ZnO distribution on the CSB surface. XPS was performed in a custom-made SPECS Surface Nano Analysis GmbH instrument using a magnesium Kα X-ray source (excitation energy output 1254 eV) with an impingement area of approximately 1 mm in diameter. XPS spectra were calibrated with reference to the Ag $3d_{5/2}$ peak position (centered at 368.10 eV) obtained from silver polycrystalline foil cleaned via standard argon ion sputtering treatment. A TGA instrument was used to investigate the thermal stability of CSB and ZCSB using a Malvern PANalytical instrument (Netherlands). The surface area and pore distribution of the samples were determined using a Nova 1200 e Quantachrome instrument (USA) with N_2 physisorption at 77 K. The samples were degassed at 343 K for 24 h. UV−Vis DR spectroscopy (Agilent Cary 60 UV−vis/DRS, USA) was employed to demonstrate the photon light absorption behavior of the samples, followed by the Tauc plot analysis to determine the band gap energy of ZCSB.

4.5. Adsorption Performance of CSB. The adsorption performance of CSB was investigated after 30 min in the dark condition. Various masses of sample were added to 20 mL of 100 mg L^{-1} MO solution under constant stirring. The filtrate was separated by centrifugation and measured with a UV−Vis spectrophotometer (Thermo Scientific Genesys 840−208100, USA). Eqs 10 and 11 were used to determine the adsorption efficiency and adsorption capacity of SB and CSB, respectively. The effect of the dosage was also studied. The result of the adsorption dosage study is also important to determine the dosage for the photocatalytic process.

$$\text{Adsorption efficiency} = \frac{C_i - C_f}{C_i} \times 100\% \tag{10}$$

$$Q = \frac{(C_i - C_f)}{m} \times V \tag{11}$$

where C_i and C_f are the initial and final concentrations of the MO solution, respectively. Q is the adsorption capacity (mg g^{-1}), m is the adsorbent mass (g), and V is the adsorbate volume (L). To compare the CSB adsorption performance, the adsorption performance of SB was also investigated under conditions similar to those in the CSB adsorption tests. However, the mass of SB was determined only at the lowest and optimum masses of CSB.

4.6. Photocatalytic Evaluation of ZCSB. Photocatalytic activity was conducted by a 50 mL batch reactor that was fulfilled with a UV-LED lamp (λ = 365 nm, p = 12 W). The UV-LED lamp was arranged in a circular manner and equipped with a cooling system around the circle. ZCSB (0.01 g) was added to 20 mL of MO solution (100 mg L^{-1}). This dosage was considered by the adsorption dosage study. The photocatalytic process is observed when the remaining dye concentration is >50% after the adsorption process. The reaction mixture was left under UV-LED irradiation for contact times of 1, 2, 3, 4, and 5 h. The absorbance of the filtrate after the reaction was measured by using a UV−vis spectrophotometer at the peak MO absorption wavelength of 465 nm. A control experiment was also carried out for 5 h in dark condition.

4.7. Influence of H_2O_2 on the Photocatalytic Activity of 10ZCSB. The influence of H_2O_2 on the photocatalytic activity of 10ZCSB was studied by the addition of 6.67 mL of H_2O_2. To generate a similar concentration of MO at a total volume of 20 mL, the MO concentration was increased to 150 mg L^{-1}. The MO solution, 10ZCSB (0.01 g), and H_2O_2 were

https://doi.org/10.1021/acsomega.4c02938
ACS Omega 2024, 9, 25251−25264

mixed and left under UV-LED irradiation for contact times similar to those used above. The obtained filtrate was analyzed by UV−Vis spectrophotometry.

4.8. Influence of the pH of the MO Solution on the Photocatalytic Activity of 10ZCSB. The influence of pH was observed by addition of 0.5 M HCl and 0.5 M NaOH to adjust the pH of the solution to acidic and basic conditions. We adjusted the pH of the MO solution to three conditions: 3, natural (pH = 6.5), and 9. The pH-adjusted MO solution was mixed with 0.01 g of 10ZCSB and irradiated for 5 h. To control the photocatalytic process, we also investigated the dark reaction under similar conditions. The filtrates obtained after irradiation and under dark conditions were measured by a UV−Vis spectrophotometer.

4.9. Influence of Ionic Strength in the MO and MB Photocatalytic Using 10ZCSB. The influence of ionic strength was observed by the addition 50 mg L^{-1} of $NaNO_3$, Na_2CO_3, and NaCl solution. The dye solution containing $NaNO_3$ solution was mixed with 0.01 g of 10ZCSB and irradiated for 5 h. To control the photocatalytic process, the dark reaction was also investigated under similar conditions. The filtrates obtained after irradiation and under dark conditions were measured by UV−Vis spectrophotometer.

AUTHOR INFORMATION

Corresponding Author

Yuly Kusumawati − *Department of Chemistry, Faculty of Science and Data Analytics, Institut Teknologi Sepuluh Nopember, Surabaya, Sukolilo 60111, Indonesia;* orcid.org/0000-0002-2079-3584; Email: y_kusumawati@chem.its.ac.id

Authors

Riki Subagyo − *Department of Chemistry, Faculty of Science and Data Analytics, Institut Teknologi Sepuluh Nopember, Surabaya, Sukolilo 60111, Indonesia;* orcid.org/0000-0002-7622-9114

Achmad R. Diakana − *Department of Chemistry, Faculty of Science and Data Analytics, Institut Teknologi Sepuluh Nopember, Surabaya, Sukolilo 60111, Indonesia*

Garcelina R. Anindika − *Department of Chemistry, Faculty of Science and Data Analytics, Institut Teknologi Sepuluh Nopember, Surabaya, Sukolilo 60111, Indonesia;* orcid.org/0009-0008-2495-9546

Syafsir Akhlus − *Department of Chemistry, Faculty of Science and Data Analytics, Institut Teknologi Sepuluh Nopember, Surabaya, Sukolilo 60111, Indonesia*

Hendro Juwono − *Department of Chemistry, Faculty of Science and Data Analytics, Institut Teknologi Sepuluh Nopember, Surabaya, Sukolilo 60111, Indonesia*

Lei Zhang − *Department of Physics, National University of Singapore, Singapore 117551, Singapore;* orcid.org/0000-0001-5112-6189

Arramel − *Center of Excellence Applied Physics and Chemistry, Nano Center Indonesia, South Tangerang, Banten 15314, Indonesia;* orcid.org/0000-0003-4125-6099

Complete contact information is available at: https://pubs.acs.org/10.1021/acsomega.4c02938

Author Contributions

R.S. wrote the original draft. A.R.D. synthesized the materials and performed the application. G.R.A. prepared the materials and performed the FTIR analysis. S.A. and H.J. reviewed and edited the draft. L.Z. and Arramel performed XPS analysis. Y.K. conceived and supervised the project. All authors have given their approval to the final manuscript version.

Funding

This research is funded by Institut Teknologi Sepuluh Nopember through the scientific research scheme No 1697/PKS/ITS/2023.

Notes

The authors declare no competing financial interest.

ACKNOWLEDGMENTS

Institut Teknologi Sepuluh Nopember is acknowledged for funding this research. The authors also acknowledged Prof. Andrew T. S. Wee (National University of Singapore) to use his XPS set up in Surface Science Laboratory.

REFERENCES

(1) Katheresan, V.; Kansedo, J.; Lau, S. Y. Efficiency of Various Recent Wastewater Dye Removal Methods: A Review. *J. Environ. Chem. Eng.* **2018**, *6* (4), 4676−4697.

(2) Gao, Q.; Xu, J.; Bu, X. H. Recent Advances about Metal−Organic Frameworks in the Removal of Pollutants from Wastewater. *Coord. Chem. Rev.* **2019**, *378*, 17−31.

(3) Tambat, S. N.; Sane, P. K.; Suresh, S.; Varadan, O. N.; Pandit, A. B.; Sontakke, S. M. Hydrothermal Synthesis of NH_2-UiO-66 and Its Application for Adsorptive Removal of Dye. *Adv. Powder Technol.* **2018**, *29* (11), 2626−2632.

(4) Subagyo, R.; Tehubijuluw, H.; Prasetyo Utomo, W.; Dwi Rizqi, H.; Kusumawati, Y.; Bahruji, H.; Prasetyoko, D. Converting Red Mud Wastes into Mesoporous ZSM-5 Decorated with TiO_2 as an Eco-Friendly and Efficient Adsorbent-Photocatalyst for Dyes Removal. *Arabian J. Chem.* **2022**, *15* (5), 103754.

(5) Sriram, G.; Bendre, A.; Altalhi, T.; Jung, H. Y.; Hegde, G.; Kurkuri, M. Surface Engineering of Silica Based Materials with Ni−Fe Layered Double Hydroxide for the Efficient Removal of Methyl Orange: Isotherms, Kinetics, Mechanism and High Selectivity Studies. *Chemosphere* **2022**, *287* (P1), 131976.

(6) Sriram, G.; Kigga, M.; Uthappa, U. T.; Rego, R. M.; Thendral, V.; Kumeria, T.; Jung, H. Y.; Kurkuri, M. D. Naturally Available Diatomite and Their Surface Modification for the Removal of Hazardous Dye and Metal Ions: A Review. *Adv. Colloid Interface Sci.* **2020**, *282*, 102198.

(7) Crini, G.; Lichtfouse, E. Advantages and Disadvantages of Techniques Used for Wastewater Treatment. *Environ. Chem. Lett.* **2019**, *17* (1), 145−155.

(8) Selvaraj, V.; Swarna Karthika, T.; Mansiya, C.; Alagar, M. An Over Review on Recently Developed Techniques, Mechanisms and Intermediate Involved in the Advanced Azo Dye Degradation for Industrial Applications. *J. Mol. Struct.* **2021**, *1224*, 129195.

(9) Saravanan, A.; Senthil Kumar, P.; Jeevanantham, S.; Karishma, S.; Tajsabreen, B.; Yaashikaa, P. R.; Reshma, B. Effective Water/Wastewater Treatment Methodologies for Toxic Pollutants Removal: Processes and Applications towards Sustainable Development. *Chemosphere* **2021**, *280*, 130595.

(10) Khan, F. S. A.; Mubarak, N. M.; Tan, Y. H.; Khalid, M.; Karri, R. R.; Walvekar, R.; Abdullah, E. C.; Nizamuddin, S.; Mazari, S. A. A Comprehensive Review on Magnetic Carbon Nanotubes and Carbon Nanotube-Based Buckypaper for Removal of Heavy Metals and Dyes. *J. Hazard. Mater.* **2021**, *413*, 125375.

(11) Fujishima, A.; Zhang, X.; Tryk, D. A. TiO_2 Photocatalysis and Related Surface Phenomena. *Surf. Sci. Rep.* **2008**, *63* (12), 515−582.

(12) Zouzelka, R.; Kusumawati, Y.; Remzova, M.; Rathousky, J.; Pauporté, T. Photocatalytic Activity of Porous Multiwalled Carbon Nanotube-TiO_2 Composite Layers for Pollutant Degradation. *J. Hazard. Mater.* **2016**, *317*, 52−59.

(13) Pant, B.; Pant, H. R.; Barakat, N. A. M.; Park, M.; Jeon, K.; Choi, Y.; Kim, H. Y. Carbon Nanofibers Decorated with Binary

https://doi.org/10.1021/acsomega.4c02938
ACS Omega 2024, 9, 25251−25264

Semiconductor (TiO_2/ZnO) Nanocomposites for the Effective Removal of Organic Pollutants and the Enhancement of Antibacterial Activities. *Ceram. Int.* **2013**, *39* (6), 7029−7035.
(14) Raza, W.; Faisal, S. M.; Owais, M.; Bahnemann, D.; Muneer, M. Facile Fabrication of Highly Efficient Modified ZnO Photocatalyst with Enhanced Photocatalytic, Antibacterial and Anticancer Activity. *RSC Adv.* **2016**, *6*, 78335−78350.
(15) Swati; Verma, R.; Chauhan, A.; Shandilya, M.; Li, X.; Kumar, R.; Kulshrestha, S. Antimicrobial Potential of Ag-Doped ZnO Nanostructure Synthesized by the Green Method Using *Moringa Oleifera* Extract. *J. Environ. Chem. Eng.* **2020**, *8* (3), 103730.
(16) Zulfa, L. L.; Ediati, R.; Hidayat, A. R. P.; Subagyo, R.; Faaizatunnisa, N.; Kusumawati, Y.; Hartanto, D.; Widiastuti, N.; Utomo, W. P.; Santoso, M. Synergistic Effect of Modified Pore and Heterojunction of MOF-Derived α-Fe_2O_3/ZnO for Superior Photocatalytic Degradation of Methylene Blue. *RSC Adv.* **2023**, *13* (6), 3818−3834.
(17) Ayu, D. G.; Gea, S.; Andriayani; Telaumbanua, D. J.; Piliang, A. F. R.; Harahap, M.; Yen, Z.; Goei, R.; Tok, A. I. Y. Photocatalytic Degradation of Methylene Blue Using N-Doped ZnO/Carbon Dot (N-ZnO/CD) Nanocomposites Derived from Organic Soybean. *ACS Omega* **2023**, *8* (17), 14965−14984.
(18) Wellia, D. V.; Kusumawati, Y.; Diguna, L. J.; Amal, M. I. Introduction of Nanomaterials for Photocatalysis. In *Nanocomposites for Visible Light-induced Photocatalysis*, Khan, M. M.; Pradhan, D.; Sohn, Y., Eds; Springer: Cham, 2017; pp. 117. .
(19) Abebe, B.; Murthy, H. C. A.; Amare, E. Enhancing the Photocatalytic Efficiency of ZnO: Defects, Heterojunction, and Optimization. *Environ. Nanotechnol., Monit. Manage.* **2020**, *14*, 100336.
(20) Prasetyoko, D.; Sholeha, N. A.; Subagyo, R.; Ulfa, M.; Bahruji, H.; Holilah, H.; Pradipta, M. F.; Jalil, A. A. Mesoporous ZnO Nanoparticles Using Gelatin — Pluronic F127 as a Double Colloidal System for Methylene Blue Photodegradation. *Korean J. Chem. Eng.* **2023**, *40* (1), 112−123.
(21) Chen, C.; Bi, W.; Xia, Z.; Yuan, W.; Li, L. Hydrothermal Synthesis of the $CuWO_4$/ZnO Composites with Enhanced Photocatalytic Performance. *ACS Omega* **2020**, *5* (22), 13185−13195.
(22) Gang, R.; Xu, L.; Xia, Y.; Zhang, L.; Wang, S.; Li, R. Facile One-Step Production of 2D/2D ZnO/RGO Nanocomposites under Microwave Irradiation for Photocatalytic Removal of Tetracycline. *ACS Omega* **2021**, *6* (5), 3831−3839.
(23) Subagyo, R.; Yudhowijoyo, A.; Sholeha, N. A.; Hutagalung, S. S.; Prasetyoko, D.; Birowosuto, M. D.; Arramel, A.; Jiang, J.; Kusumawati, Y. Recent Advances of Modification Effect in Co_3O_4-Based Catalyst towards Highly Efficient Photocatalysis. *J. Colloid Interface Sci.* **2023**, *650* (PB), 1550−1590.
(24) Wellia, D. V.; Kusumawati, Y.; Diguna, L. J.; Pratiwi, N.; Putri, R. A.; Amal, M. I. Mesoporous Materials for Degradation of Textile Dyes. In *Green Methods for Wastewater Treatment*, Naushad, M.; Srivastava, R.; Lichtfouse, E., Eds; Springer: Cham, 2020; pp. 255288. .
(25) Calzada, L. A.; Castellanos, R.; García, L. A.; Klimova, T. E. TiO_2, SnO_2 and ZnO Catalysts Supported on Mesoporous SBA-15 versus Unsupported Nanopowders in Photocatalytic Degradation of Methylene Blue. *Microporous Mesoporous Mater.* **2019**, *285* (May), 247−258.
(26) Tehubijuluw, H.; Subagyo, R.; Kusumawati, Y.; Prasetyoko, D. The Impregnation of ZnO onto ZSM-5 Derived from Red Mud for Photocatalytic Degradation of Methylene Blue. *Sustain. Environ. Res.* **2022**, *32*, 1−12.
(27) Nasrollahzadeh, M. S.; Hadavifar, M.; Ghasemi, S. S.; Arab Chamjangali, M. Synthesis of ZnO Nanostructure Using Activated Carbon for Photocatalytic Degradation of Methyl Orange from Aqueous Solutions. *Appl. Water Sci.* **2018**, *8* (4), 1−12.
(28) *U.N. International Decade for Action on Water for Sustainable Development*. https://www.un.org/en/events/waterdecade/ (accessed 2022−05−06).
(29) Batista, G.; Souza, R. B. A.; Pratto, B.; dos Santos-Rocha, M. S. R.; Cruz, A. J. G. Effect of Severity Factor on the Hydrothermal Pretreatment of Sugarcane Straw. *Bioresour. Technol.* **2019**, *275*, 321−327.
(30) Zhang, Z.; Moghaddam, L.; O'Hara, I. M.; Doherty, W. O. S. Congo Red Adsorption by Ball-Milled Sugarcane Bagasse. *Chem. Eng. J.* **2011**, *178*, 122−128.
(31) Ntakirutimana, S.; Tan, W.; Wang, Y. Enhanced Surface Activity of Activated Carbon by Surfactants Synergism. *RSC Adv.* **2019**, *9* (45), 26519−26531.
(32) Tang, Z.; Peng, S.; Hu, S.; Hong, S. Enhanced Removal of Bisphenol-AF by Activated Carbon-Alginate Beads with Cetyltrimethyl Ammonium Bromide. *J. Colloid Interface Sci.* **2017**, *495*, 191−199.
(33) García, M. T.; Ribosa, I.; Guindulain, T.; Sánchez-Leal, J.; Vives-Rego, J. Fate and Effect of Monoalkyl Quaternary Ammonium Surfactants in the Aquatic Environment. *Environ. Pollut.* **2001**, *111* (1), 169−175.
(34) Rovani, S.; Santos, J. J.; Guilhen, S. N.; Corio, P.; Fungaro, D. A. Fast, efficient and clean adsorption of bisphenol-A using renewable mesoporous silica nanoparticles from sugarcane waste ash. *RSC Adv.* **2020**, *10* (46), 27706−27712.
(35) Asranudin; Purnomo, A. S.; Prasetyoko, D.; Bahruji, H.; Holilah. Single-Step Synthesis and Modification of CTAB-Hectorite for Efficient Adsorption of Methyl Orange Dye. *Mater. Chem. Phys.* **2022**, *291*, 126749.
(36) Asranudin, N.; Holilah, N.; Purnomo, A. S.; Bahruji, H.; Allouss, D.; El Alaoui-Elbalrhiti, I.; Subagyo, R.; Rohmah, A. A.; Prasetyoko, D. Hectorite-CTAB-Alginate Composite Beads for Water Treatment: Kinetic, Isothermal and Thermodynamic Studies. *RSC Adv.* **2023**, *13* (2), 790−801.
(37) Ma, Z.; Yang, Y.; Ma, Q.; Zhou, H.; Luo, X.; Liu, X.; Wang, S. Evolution of the Chemical Composition, Functional Group, Pore Structure and Crystallographic Structure of Bio-Char from Palm Kernel Shell Pyrolysis under Different Temperatures. *J. Anal. Appl. Pyrolysis* **2017**, *127* (38), 350−359.
(38) Luo, L.; Xu, C.; Chen, Z.; Zhang, S. Properties of Biomass-Derived Biochars: Combined Effects of Operating Conditions and Biomass Types. *Bioresour. Technol.* **2015**, *192*, 83−89.
(39) Wiercigroch, E.; Szafraniec, E.; Czamara, K.; Pacia, M. Z.; Majzner, K.; Kochan, K.; Kaczor, A.; Baranska, M.; Malek, K. Raman and Infrared Spectroscopy of Carbohydrates: A Review. *Spectrochim. Acta, Part A* **2017**, *185*, 317−335.
(40) Sun, R. C.; Tomkinson, J. Characterization of Hemicelluloses Obtained by Classical and Ultrasonically Assisted Extractions from Wheat Straw. *Carbohydr. Polym.* **2002**, *50* (3), 263−271.
(41) Oudiani, A. E.; Chaabouni, Y.; Msahli, S.; Sakli, F. Crystal Transition from Cellulose I to Cellulose II in NaOH Treated *Agave Americana* L. Fibre. *Carbohydr. Polym.* **2011**, *86* (3), 1221−1229.
(42) French, A. D. Increment in Evolution of Cellulose Crystallinity Analysis. *Cellulose* **2020**, *27* (10), 5445−5448.
(43) French, A. D. Idealized Powder Diffraction Patterns for Cellulose Polymorphs. *Cellulose* **2014**, *21* (2), 885−896.
(44) French, A. D.; Santiago Cintrón, M. Cellulose Polymorphy, Crystallite Size, and the Segal Crystallinity Index. *Cellulose* **2013**, *20* (1), 583−588.
(45) Ling, Z.; Wang, T.; Makarem, M.; Cheng, H. N.; Kang, X.; Bacher, M.; Potthast, A.; Rosenau, T.; King, H.; Delhom, C. D.; et al. Effects of Ball Milling on the Structure of Cotton Cellulose. *Cellulose* **2019**, *26* (1), 305−328.
(46) Pawar, R. R.; Patel, H. A.; Sethia, G.; Bajaj, H. C. Selective Adsorption of Carbon Dioxide over Nitrogen on Calcined Synthetic Hectorites with Tailor-Made Porosity. *Appl. Clay Sci.* **2009**, *46* (1), 109−113.
(47) Elumalai, K.; Velmurugan, S. Green Synthesis, Characterization and Antimicrobial Activities of Zinc Oxide Nanoparticles from the Leaf Extract of *Azadirachta Indica* (L.). *Appl. Surf. Sci.* **2015**, *345*, 329−336.

https://doi.org/10.1021/acsomega.4c02938
ACS Omega 2024, 9, 25251−25264

(48) Zhang, P.; Liao, W.; Kumar, A.; Zhang, Q.; Ma, H. Characterization of Sugarcane Bagasse Ash as a Potential Supplementary Cementitious Material: Comparison with Coal Combustion Fly Ash. *J. Cleaner Prod.* **2020**, *277*, 123834.
(49) Oliveira, F. B. D.; Bras, J.; Pimenta, M. T. B.; Curvelo, A. A. D. S.; Belgacem, M. N. Production of Cellulose Nanocrystals from Sugarcane Bagasse Fibers and Pith. *Ind. Crops Prod.* **2016**, *93*, 48−57.
(50) Guo, Y.; Tan, C.; Sun, J.; Li, W.; Zhang, J.; Zhao, C. Porous Activated Carbons Derived from Waste Sugarcane Bagasse for CO_2 Adsorption. *Chem. Eng. J.* **2020**, *381*, 122736.
(51) Ayiania, M.; Smith, M.; Hensley, A. J. R.; Scudiero, L.; McEwen, J.-S.; Garcia-Perez, M. Deconvoluting the XPS Spectra for Nitrogen-Doped Chars: An Analysis from First Principles. *Carbon* **2020**, *162*, 528−544.
(52) Phakkhawan, A.; Horprathum, M.; Chanlek, N.; Nakajima, H.; Nijpanich, S.; Kumnorkaew, P.; Pimanpang, S.; Klangtakai, P.; Amornkitbamrung, V. Activated Carbons Derived from Sugarcane Bagasse for High-Capacitance Electrical Double Layer Capacitors. *J. Mater. Sci.: Mater. Electron.* **2022**, *33* (2), 663−674.
(53) Xu, T.; Qiu, X.; Zhang, X.; Xia, Y. Regulation of Surface Oxygen Functional Groups and Pore Structure of Bamboo-Derived Hard Carbon for Enhanced Sodium Storage Performance. *Chem. Eng. J.* **2023**, *452*, 139514.
(54) Torrisi, L.; Silipigni, L.; Cutroneo, M.; Torrisi, A. Graphene Oxide as a Radiation Sensitive Material for XPS Dosimetry. *Vacuum* **2020**, *173*, 109175.
(55) Lekoui, F.; Amrani, R.; Filali, W.; Garoudja, E.; Sebih, L.; Bakouk, I. E.; Akkari, H.; Hassani, S.; Saoula, N.; Oussalah, S.; et al. Investigation of the Effects of Thermal Annealing on the Structural, Morphological and Optical Properties of Nanostructured Mn Doped ZnO Thin Films. *Opt. Mater.* **2021**, *118*, 111236.
(56) Sambandam, B.; Michael, R. J. V.; Manoharan, P. T. Oxygen Vacancies and Intense Luminescence in Manganese Loaded ZnO Microflowers for Visible Light Water Splitting. *Nanoscale* **2015**, *7* (33), 13935−13942.
(57) Qu, G.; Fan, G.; Zhou, M.; Rong, X.; Li, T.; Zhang, R.; Sun, J.; Chen, D. Graphene-Modified ZnO Nanostructures for Low-Temperature NO_2 Sensing. *ACS Omega* **2019**, *4* (2), 4221−4232.
(58) Lei, J.; Liu, W.; Jin, Y.; Li, B. Oxygen Vacancy-Dependent Chemiluminescence: A Facile Approach for Quantifying Oxygen Defects in ZnO. *Anal. Chem.* **2022**, *94* (24), 8642−8650.
(59) Men, S.; Lovelock, K. R. J.; Licence, P. X-Ray Photoelectron Spectroscopy of Pyrrolidinium-Based Ionic Liquids: Cation-Anion Interactions and a Comparison to Imidazolium-Based Analogues. *Phys. Chem. Chem. Phys.* **2011**, *13* (33), 15244−15255.
(60) Herranz, T.; Deng, X.; Cabot, A.; Liu, Z.; Salmeron, M. In Situ XPS Study of the Adsorption and Reactions of NO and O_2 on Gold Nanoparticles Deposited on TiO_2 and SiO_2. *J. Catal.* **2011**, *283* (2), 119−123.
(61) Xie, F.; Yang, M.; Song, Z.-Y.; Duan, W.-C.; Huang, X.-J.; Chen, S.-H.; Li, P.-H.; Xiao, X.-Y.; Liu, W.-Q.; Xie, P.-H. Highly Sensitive Electrochemical Detection of Hg(II) Promoted by Oxygen Vacancies of Plasma-Treated ZnO: XPS and DFT Calculation Analysis. *Electrochim. Acta* **2022**, *426*, 140757.
(62) Khan, Y.; Durrani, S. K.; Mehmood, M.; Ahmad, J.; Khan, M. R.; Firdous, S. Low Temperature Synthesis of Fluorescent ZnO Nanoparticles. *Appl. Surf. Sci.* **2010**, *257* (5), 1756−1761.
(63) Huang, Z.; Li, Y.; Chen, W.; Shi, J.; Zhang, N.; Wang, X.; Li, Z.; Gao, L.; Zhang, Y. Modified Bentonite Adsorption of Organic Pollutants of Dye Wastewater. *Mater. Chem. Phys.* **2017**, *202*, 266−276.
(64) Wang, Y.; Guan, J.; Li, L.; Wang, Z.; Yuan, X.; Yan, Y.; Li, X.; Lu, N. Graphite-Bridged Indirect Z-Scheme System TiO_2−C−$BiVO_4$ Film with Enhanced Photoelectrocatalytic Activity towards Serial Bisphenols. *Environ. Res.* **2020**, *191*, 110221.
(65) Gong, S.; Jiang, Z.; Zhu, S.; Fan, J.; Xu, Q.; Min, Y. The Synthesis of Graphene-TiO_2/g-C_3N_4 Super-Thin Heterojunctions with Enhanced Visible-Light Photocatalytic Activities. *J. Nanopart. Res.* **2018**, *20*, 310−323.
(66) Tehubijuluw, H.; Subagyo, R.; Yulita, M. F.; Nugraha, R. E.; Kusumawati, Y.; Bahruji, H.; Jalil, A. A.; Hartati, H.; Prasetyoko, D. Utilization of Red Mud Waste into Mesoporous ZSM-5 for Methylene Blue Adsorption-Desorption Studies. *Environ. Sci. Pollut. Res.* **2021**, *28*, 37354−37370.
(67) Santoso, E.; Ediati, R.; Istiqomah, Z.; Sulistiono, D. O.; Nugraha, R. E.; Kusumawati, Y.; Bahruji, H.; Prasetyoko, D. Facile Synthesis of ZIF-8 Nanoparticles Using Polar Acetic Acid Solvent for Enhanced Adsorption of Methylene Blue. *Microporous Mesoporous Mater.* **2021**, *310*, 110620.
(68) Martak, F.; Hafiz, M. R. A.; Sulistiono, D. O.; Rosyidah, A.; Kusumawati, Y.; Ediati, R. Direct Synthesis of Al-HKUST-1 and Its Application as Adsorbent for Removal of Congo Red in Water. *Nano-Struct. Nano-Objects* **2021**, *27*, 100773.
(69) Zhai, L.; Bai, Z.; Zhu, Y.; Wang, B.; Luo, W. Fabrication of Chitosan Microspheres for Efficient Adsorption of Methyl Orange. *Chin. J. Chem. Eng.* **2018**, *26* (3), 657−666.
(70) Yao, W.; Yu, S.; Wang, J.; Zou, Y.; Lu, S.; Ai, Y.; Alharbi, N. S.; Alsaedi, A.; Hayat, T.; Wang, X. Enhanced Removal of Methyl Orange on Calcined Glycerol-Modified Nanocrystallined Mg/Al Layered Double Hydroxides. *Chem. Eng. J.* **2017**, *307*, 476−486.
(71) Zhou, Q.; Chen, F.; Wu, W.; Bu, R.; Li, W.; Yang, F. Reactive Orange 5 Removal from Aqueous Solution Using Hydroxyl Ammonium Ionic Liquids/Layered Double Hydroxides Intercalation Composites. *Chem. Eng. J.* **2016**, *285*, 198−206.
(72) Sahu, S.; Pahi, S.; Tripathy, S.; Singh, S. K.; Behera, A.; Sahu, U. K.; Patel, R. K. Adsorption of Methylene Blue on Chemically Modified Lychee Seed Biochar: Dynamic, Equilibrium, and Thermodynamic Study. *J. Mol. Liq.* **2020**, *315*, 113743.
(73) Zhang, Q.; Cheng, Y.; Fang, C.; Chen, J.; Chen, H.; Li, H.; Yao, Y. Facile Synthesis of Porous Carbon/Fe_3O_4 Composites Derived from Waste Cellulose Acetate by One-Step Carbothermal Method as a Recyclable Adsorbent for Dyes. *J. Mater. Res. Technol.* **2020**, *9* (3), 3384−3393.
(74) Tang, X.; Ran, G.; Li, J.; Zhang, Z.; Xiang, C. Extremely Efficient and Rapidly Adsorb Methylene Blue Using Porous Adsorbent Prepared from Waste Paper: Kinetics and Equilibrium Studies. *J. Hazard. Mater.* **2021**, *402*, 123579.
(75) Mahmoodi, N. M.; Arami, M.; Limaee, N. Y.; Tabrizi, N. S. Kinetics of Heterogeneous Photocatalytic Degradation of Reactive Dyes in an Immobilized TiO_2 Photocatalytic Reactor. *J. Colloid Interface Sci.* **2006**, *295* (1), 159−164.
(76) Truong, H. B.; Huy, B. T.; Ray, S. K.; Lee, Y.-I.; Cho, J.; Hur, J. H_2O_2-Assisted Photocatalysis for Removal of Natural Organic Matter Using Nanosheet C_3N_4-WO_3 Composite under Visible Light and the Hybrid System with Ultrafiltration. *Chem. Eng. J.* **2020**, *399*, 125733.
(77) Degabriel, T.; Colaço, E.; Domingos, R. F.; El Kirat, K.; Brouri, D.; Casale, S.; Landoulsi, J.; Spadavecchia, J. Factors Impacting the Aggregation/Agglomeration and Photocatalytic Activity of Highly Crystalline Spheroid- and Rod-Shaped TiO_2 Nanoparticles in Aqueous Solutions. *Phys. Chem. Chem. Phys.* **2018**, *20* (18), 12898−12907.
(78) Brüninghoff, R.; Van Duijne, A. K.; Braakhuis, L.; Saha, P.; Jeremiasse, A. W.; Mei, B.; Mul, G. Comparative Analysis of Photocatalytic and Electrochemical Degradation of 4-Ethylphenol in Saline Conditions. *Environ. Sci. Technol.* **2019**, *53* (15), 8725−8735.
(79) Hassan, N. S.; Jalil, A. A.; Triwahyono, S.; Hitam, C. N. C.; Rahman, A. F. A.; Khusnun, N. F.; Mamat, C. R.; Asmadi, M.; Mohamed, M.; Ali, M. W.; et al. Exploiting Copper−Silica−Zirconia Cooperative Interactions for the Stabilization of Tetragonal Zirconia Catalysts and Enhancement of the Visible-Light Photodegradation of Bisphenol A. *J. Taiwan Inst. Chem. Eng.* **2018**, *82*, 322−330.
(80) Fauzi, A. A.; Jalil, A. A.; Hassan, N. S.; Aziz, F. F. A.; Azami, M. S.; Abdullah, T. A. T.; Kamaroddin, M. F. A.; Setiabudi, H. D. An Intriguing Z-Scheme Titania Loaded on Fibrous Silica Ceria for Accelerated Visible-Light-Driven Photocatalytic Degradation of Ciprofloxacin. *Environ. Res.* **2022**, *211*, 113069.
(81) Gaber, M. M.; Samy, M.; El-Bestawy, E. A.; Shokry, H. Effective Degradation of Tetracycline and Real Pharmaceutical Wastewater

https://doi.org/10.1021/acsomega.4c02938
ACS Omega 2024, 9, 25251−25264

Using Novel Nanocomposites of Biosynthesized ZnO and Carbonized Toner Powder. *Chemosphere* **2024**, *352*, 141448.
(82) Azami, M. S.; Jalil, A. A.; Aziz, F. F. A.; Hassan, N. S.; Mamat, C. R.; Izzudin, N. M. Influence of the Nitrogen Pots from Graphitic Carbon Nitride with the Presence of Wrinkled Silica-Titania for Photodegradation Enhancement of 2-Chlorophenol. *Int. J. Hydrogen Energy* **2023**, *48* (17), 6532−6545.

https://doi.org/10.1021/acsomega.4c02938
ACS Omega 2024, 9, 25251−25264